Neutrino-oscillation experiments at the Gösgen nuclear power reactor

G. Zacek,* F. v. Feilitzsch, R. L. Mössbauer, L. Oberauer, and V. Zacek*
Physik Department, Technische Universität München, D-8046 Garching, Federal Republic of Germany

F. Boehm, P. H. Fisher,† J. L. Gimlett,‡ A. A. Hahn,§ H. E. Henrikson, H. Kwon,** and J. L. Vuilleumier††
California Institute of Technology, Pasadena, California 91125

K. Gabathuler
Schweizerisches Institut für Nuklearforschung, CH-5234 Villigen, Switzerland
(Caltech-SIN-TUM Collaboration)
(Received 3 April 1986)

A search for neutrino oscillations has been conducted at the 2800-MW (thermal) nuclear power reactor in Gösgen (Switzerland), providing 5×10^{20} electron antineutrinos per second. The energy spectrum of the antineutrinos was measured at three distances, 37.9, 45.9, and 64.7 m, from the reactor core. The detection of the neutrinos is based on the reaction $\bar{\nu}_e+p\rightarrow e^++n$. Roughly 10^4 antineutrinos were registered at each of the three measuring positions. The measured spectra are analyzed in terms of a two-neutrino oscillation model and the results are represented as exclusion plots for the oscillation parameters Δm^2 and $\sin^2 2\theta$. Two analyses are performed: Analysis A relies exclusively on the data measured at the three different distances; analysis B combines the measured data with additional information, in particular with the reactor antineutrino spectrum as derived from independent β-spectroscopic measurements. Both analyses show that the data are consistent with the absence of neutrino oscillations, and rule out large regions of parameters $(\Delta m^2,\theta)$. The resulting limits on the oscillation parameters are $\Delta m^2<0.019$ eV^2 (90% C.L.) for maximum mixing and $\sin^2 2\theta<0.21$ (90% C.L.) for $\Delta m^2>5$ eV^2.

I. INTRODUCTION

The question whether the neutrino possesses a finite rest mass and the problem of neutrino mixing remains one of the most important and challenging issues in today's physics. Measurements of two-body and three-body weak decays so far provide only rather large upper limits on the masses of the participating neutrinos: $m(\bar{\nu}_e)<60$ eV (Ref. 1), $m(\nu_\mu)<250$ keV (Ref. 2), and $m(\nu_\tau)<84$ MeV (Ref. 3). [One experiment provides an as yet unconfirmed value for the mass of the electron antineutrino: $m(\bar{\nu}_e)>20$ eV (Ref. 4).] Studies of neutrinoless double-β decay likewise lead to limits on neutrino masses, assuming that neutrinos are Majorana particles.[5] A knowledge of neutrino masses would provide important input parameters for elementary-particle theories and might have severe consequences for astrophysics and cosmology. Some versions of grand unified theories of elementary-particle interactions, for example, the minimal SU(5) model, provide no room for processes generating neutrino masses. In more extended theories such as SO(10), neutrinos may indeed acquire mass and a wide range of mass values from 10^{-6} up to 10 eV might be possible. Neutrinos with masses in the 10-eV range would contribute substantially to the dark matter in the Universe and might even lead to a closed universe.

The questions of neutrino mass and of lepton-number conservation are closely related. According to our present understanding baryon and lepton numbers might not be exactly conserved. A violation of lepton-number conservation together with the existence of nonzero neutrino masses can give rise to the phenomenon of neutrino oscillations as first discussed by Pontecorvo;[6] i.e., the eigenstates as created and detected in weak-interaction processes are linear superpositions of neutrino mass eigenstates. More recently neutrino mixing was also proposed on theoretical grounds within the framework of grand-unified theories. Such a process might be at the origin of the observed deficit in the solar-neutrino flux.[7]

In this paper we report on a search for neutrino oscillations performed at the nuclear power reactor in Gösgen, Switzerland. The energy spectra of the electron antineutrinos emerging from the reactor core have been measured at distances of $L_1=37.9$ m (experiment I), $L_2=45.9$ m (experiment II), and $L_3=64.7$ m (experiment III).

The measured spectra are analyzed in terms of a two-neutrino-oscillation model. Two analyses are presented. (A) The first is based exclusively on a comparison of the measured spectra obtained at the three distances L_j. This analysis is essentially independent of any external assumptions concerning the reactor antineutrino spectrum, the detection cross section, and the detector efficiency. (B) The second analysis includes the reactor antineutrino spectrum as derived from independent β-spectroscopic measurements. This procedure increases our sensitivity to the oscillation parameters.

Short reports of our work at Gösgen are presented in Refs. 8, 9, and 10. Previous measurements performed at the Institut Laue-Langevin (ILL) reactor in Grenoble, France at $L=8.76$ m are published in Ref. 11 and are consistent with the results reported here.

II. NEUTRINO MIXING AND NEUTRINO OSCILLATIONS

Neutrino mixing assumes a linear relation between the weak-interaction eigenstates ν_α ($\alpha=e,\mu,\tau,\ldots$) and the mass eigenstates ν_j ($j=1,2,3,\ldots$):

$$|\nu_\alpha\rangle=\sum_j U_{\alpha,j}|\nu_j\rangle\ , \tag{1}$$

where $U_{\alpha,j}$ represents a unitary mixing matrix. Information on mixing parameters $U_{\alpha,j}$ and on neutrino mass eigenvalues m_j can be obtained by kinematic studies such as a search for additional peaks or shoulders in the momentum distribution of charged leptons emitted in weak decays.[12] These anomalies are related to the mass values m_j of the admixed mass eigenstates and to the degree of admixture $U_{\alpha,j}$. Extensive searches for neutrino decay have also provided limits on the mixing parameters.[13] Furthermore one can also exploit the time dependence of the neutrino states ν_α, which gives rise to the phenomenon of neutrino oscillations. If the neutrino state ν_α is created at the time $t=0$ with momentum p, its time development is

$$|\nu_\alpha(t)\rangle=\sum_j U_{\alpha,j}\exp[-i(p+m_j{}^2/2p)t]\,|\nu_j\rangle\ . \tag{2}$$

Here it is assumed that the mass eigenvalues $m_j \ll p$. In a weak decay, a neutrino is emitted in a definite state ν_α. The probability of finding this neutrino at distance $L\approx ct$ (in m) in a state ν_β is given by

$$P_{\alpha,\beta}=\sum_k\sum_l U^\dagger{}_{\alpha,k}U_{\beta,k}U^\dagger{}_{\alpha,l}U_{\beta,l}\cos(2.53\Delta m^2{}_{k,l}L/E_\nu)\ , \tag{3}$$

where E_ν is the neutrino energy (in MeV) and $\Delta m^2{}_{k,l}=|m_k{}^2-m_l{}^2|$ (in eV^2). It is evident from Eq. (3) that oscillation experiments do not measure neutrino masses themselves, but instead are sensitive to differences of squares of neutrino mass eigenvalues. The mass parameters $\Delta m^2{}_{k,l}$ determine the spatial periodicities of the observable intensity pattern of the measured neutrino spectrum, while the mixing parameters $U_{\alpha,j}$ govern the oscillation amplitude.

Equation (3) applies to two types of oscillation experiments.

(1) Appearance experiments search for neutrino states ν_β, which were not present in the initial beam of ν_α. These experiments are in principle very sensitive to mixing parameters, however, the limitation being the contamination of the initial beam of neutrinos of type ν_β and the statistics. Such experiments explore only the particular oscillation channel under study ($\alpha\leftrightarrow\beta$).

(2) Disappearance experiments search for intensity reductions in the primary neutrino beam ν_α due to losses of neutrinos by oscillations into other weak-interaction neutrino states before detection. The loss factor is given by $1-P_{\alpha,\alpha}$ [Eq. (3)]. Such experiments, although sensitive to several oscillation channels simultaneously, must rely on the knowledge of the neutrino spectrum at t (or L) $=0$, the energy distribution and normalization of which may be difficult to obtain. This situation improves substantially if measurements are performed at different distances L between source and detector under otherwise equivalent conditions. Disappearance experiments, nevertheless, are not very sensitive to small mixing angles.

A two-neutrino mixing model (apart from very special relations between the mass eigenvalues m_j) represents a good approximation to the general case (3). Here the mixing parameters $U_{\alpha,j}$ are elements of a two-dimensional unitary matrix, which is parametrized by a single mixing angle θ:

$$U_{\alpha,j}=\begin{pmatrix}\cos\theta & \sin\theta\\ -\sin\theta & \cos\theta\end{pmatrix}\ . \tag{4}$$

The probability of finding the original weak-interaction neutrino state at a distance L from the source follows from Eq. (3):

$$P(E_\nu,L,\Delta m^2,\theta)=1-\sin^2 2\theta\sin^2(1.27\Delta m^2 L/E_\nu)\ . \tag{5}$$

Experimental studies of neutrino oscillations aim at a determination of the mass parameter $\Delta m^2=|m_1{}^2-m_2{}^2|$ and the mixing parameter $\sin^2 2\theta$. These parameters can be obtained from measurements at different energies E_ν and distances L. According to Eq. (5) maximum sensitivity to the mass parameter is obtained for $\Delta m^2\approx E_\nu/L$. In practice the energy resolution of the neutrino detector will limit the sensitivity to large values of Δm^2, whereas the value E_ν/L determines the sensitivity to smaller mass parameter values. The relatively low neutrino energies available and the small distances applicable ($L/E_\nu\approx 10$ m/MeV) make oscillation experiments at fission reactors particularly sensitive to the domain of small mass parameters Δm^2 in the range of 0.01 to 1 eV^2.

III. NEUTRINO SOURCE AND NEUTRINO DETECTION REACTION

A. The electron antineutrino spectrum of a nuclear reactor

During fission in a nuclear reactor, unstable neutron-rich isotopes are created which subsequently undergo β^- decays. Each decay is accompanied by the emission of an electron antineutrino. A nuclear reactor is thus an intense source of electron antineutrinos.

The power reactor at Gösgen, a pressurized light water reactor with an average thermal power of 2800 MW, constitutes a neutrino source with a total flux of 5×10^{20} $\bar{\nu}_e$/sec and with energies up to 8 MeV. This commercially used reactor operates for a period of about 11 months, followed by a shutdown of one month to allow for the replacement of one-third of the fuel elements. At the beginning of each annual cycle 69% of the fissions are from ^{235}U, 7% from ^{238}U, 21% from ^{239}Pu, and 3% from ^{241}Pu. During operation the fissionable isotopes ^{239}Pu and ^{241}Pu are bred continuously from ^{238}U.

The contributions to the reactor power of the relevant fissioning isotopes, averaged over the measuring periods of each of the experiments I–III, are shown in Table I. The antineutrino spectra following fission of the various uranium and plutonium isotopes differ. For this reason, an evaluation of the time-dependent composite antineutri-

TABLE I. Contributions to the reactor power of the relevant fissioning isotopes, averaged over the measuring periods of each of the experiments I–III (Ref. 14). The average reactor power for the three measurements is also given.

Experiment	L (m)	^{235}U	^{239}Pu	^{238}U	^{241}Pu	Average thermal reactor power (MW)
I	37.9	61.9%	27.2%	6.7%	4.2%	2814
II	45.9	58.4%	29.8%	6.8%	5.0%	2807
III	64.7	54.3%	32.9%	7.0%	5.8%	2802

no spectrum requires a knowledge of the contributions to the number of fissions of the various fissile isotopes as a function of time. The burn up varies along the length of a fuel element, because the neutron flux is smaller at the two ends. For evaluating the time dependence, each of the 177 fuel elements was therefore subdivided in length into 30 segments. The number $n_i^j(t)$ of fissions per second and per segment j for each isotope i is then given by

$$n_i^j(t)=\alpha^j(t)b_i(A)W(t)/\sum_i b_i(A)E_i^{\text{eff}} , \tag{6}$$

where $\alpha^j(t)$ is the known relative power contribution of segment j ($j=1,\ldots,30$), $b_i(A)$ is the relative contribution of isotope i to the number of fissions, which is a function of the burn up A (MW day per ton of U). Both functions $\alpha^j(t)$ and $b_i(A)$ were obtained in tabulated form from the power station.[14] $W(t)$ is the daily average power and E_i^{eff} is the effective energy release per fission. For a specific isotope i, the quantity E_i^{eff} is a sum of contributions due to the fission process itself, due to successive β decays and due to neutron capture in the surrounding material. The values for E_i^{eff}, taken from Ref. 15 amount to 201.7±0.6 MeV (^{235}U), 205.0±0.9 MeV (^{238}U), 210.0±0.9 MeV (^{239}Pu), and 212.4±1.0 MeV (^{241}Pu). The contribution of a single fuel element to the total number of fissions for each individual isotope i is obtained by summing $n_i^j(t)$ over all fuel element segments j and by integrating over the actual time of measurement. Adding the contribution of all fuel elements and averaging over the effective data taking time yields the average number N_i of fissions per second for each isotope i for experiments I–III, which are associated with slightly different fuel element compositions. Relative contributions of the four relevant isotopes are shown in Fig. 1 for the entire period of the measurement. We have neglected the contributions from other fissioning isotopes, such as ^{236}U, ^{240}Pu, ^{242}Pu, etc., which amount to less than 0.1%.

In order to obtain the reactor antineutrino spectrum (the source spectrum), we require in addition to the average number N_i of fissions per second of each of the four isotopes, the associated neutrino yields $S_i(E_\nu)$ per MeV and fission. Since it is difficult to judge the quality of differing theoretical predictions, we have as much as possible relied on experimental data. Neutrino yields $S_i(E_\nu)$ per MeV and fission for the two dominant isotopes ^{235}U [$S_1(E_\nu)$] and ^{239}Pu [$S_2(E_\nu)$] were obtained by converting β spectra independently measured with a β spectrometer using fissioning ^{235}U and ^{239}Pu targets.[16] These yields contain a normalization error originating from the calibration uncertainty of the spectrometer and from the error in the conversion from a β to a neutrino spectrum. In establishing the uncertainty of the composite neutrino spectrum, the calibration and conversion errors were treated as correlated. For the less important isotopes ^{238}U [$S_3(E_\nu)_{\text{th}}$] and ^{241}Pu [$S_4(E_\nu)_{\text{th}}$] we have relied on calculated antineutrino spectra.[17] Because it has been noted[18] that there is much better agreement between the ratios of calculated differential neutrino yields with the experimentally determined ratios than between their absolute values, we have used for the neutrino yields $S_3(E_\nu)$ and $S_4(E_\nu)$ the quantities

$$S_{3,4}(E_\nu)=S_{3,4}(E_\nu)_{\text{th}}F(E_\nu) .$$

The correction factor is defined by

$$F(E_\nu)=0.5[(S_1/S_{1\text{th}}+S_2/S_{2\text{th}})(E_\nu)] ,$$

where $S_1/S_{1\text{th}}$ and $S_2/S_{2\text{th}}$ were found to be in good agreement. The difference between $F(E_\nu)$ and either $S_1/S_{1\text{th}}$ or $S_2/S_{2\text{th}}$ is less than 4% at all energies. The composite reactor antineutrino spectrum $S_B(E_\nu)$ is finally obtained from

$$S_B(E_\nu)=\sum_i N_iS_i(E_\nu)\ \text{MeV}^{-1}\text{sec}^{-1} . \tag{7}$$

It should be stressed that the evaluation of the reactor antineutrino spectrum $S_B(E_\nu)$ is only to a minor extent

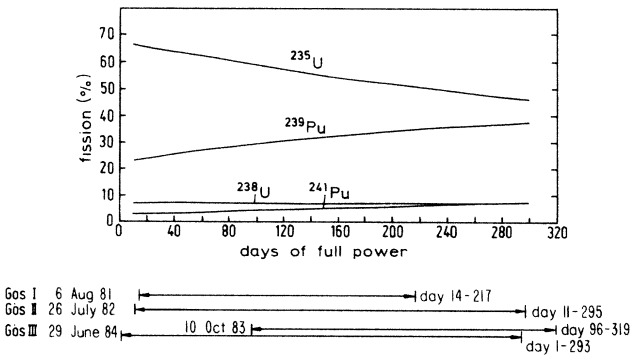

FIG. 1. Relative contributions to the number of fissions from the four relevant isotopes as a function of days of reactor at full power. The data-taking periods and starting dates of experiments I–III are indicated.

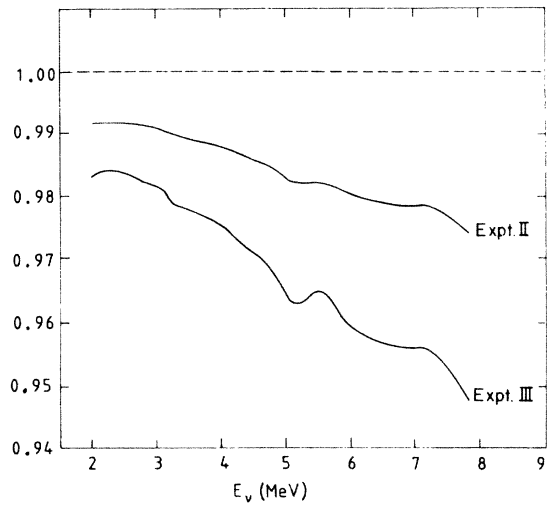

FIG. 2. Relative changes of the reactor antineutrino yields of experiments II and III, as compared to the yield of experiment I, as a function of the neutrino energy. These differences are caused by slight changes in the reactor fuel compositions and the slightly different measuring periods within the reactor cycles.

dependent on the quality of the employed theoretical models. At low energies ($E_\nu \approx 2$ MeV) there is at most a spread of 5% between the most up-to-date calculations of $S_{1,2}(E_\nu)$ (Refs. 17 and 19), while around 5 MeV the discrepancy increases to about 20%. This should not be different for $S_{3,4}$. These uncertainties, however, have to be weighted with the 10% abundance of the two isotopes ^{238}U and ^{241}Pu. Thus the spectrum $S_B(E_\nu)$ is essentially based on repeatedly checked experimental data.

Combining the experimental errors with the quoted uncertainties of the theoretical calculations, we arrive at a total uncertainty of 3.0% (68% C.L.) for the normalization of the composite neutrino spectrum. Figure 2 illustrates the changes in the time-averaged reactor antineutrino spectra for experiments I–III. To minimize the effect of differing fuel compositions, we took data during roughly equivalent periods within each reactor cycle.

B. Detection reaction and reaction cross section

The neutrino spectrum at a distance L from the reactor is obtained by measuring the positron spectrum resulting from the inverse-β-decay reaction $\bar{\nu}_e + p \rightarrow e^+ + n$. In the limit of infinite nucleon mass the energy E_ν of the incident neutrino is given by

$$E_\nu = E_{e^+} + (M_n - M_p)c^2 + m_e c^2 = E_{e^+} + 1.804 \text{ MeV} ,$$

with M_n, M_p, and m_e being the masses of neutron, proton, and electron, respectively, and E_{e^+} is the kinetic energy of the positron. The measured positron spectrum is thus essentially the antineutrino spectrum shifted in energy and weighted by the cross section. Deviations from this simple approximation due to the finite nucleon mass were taken into account as discussed in Sec. VI B.

In the limit of finite nucleon mass the cross section for the reaction $\bar{\nu}_e + p \rightarrow e^+ + n$ is given by[20]

$$\begin{aligned}\sigma(\bar{\nu}_e p \rightarrow e^+ n) = {} & 2\pi^2 \ln 2 (\hbar c)^2 \hbar / (m_e c^2)^5 f t_{1/2} \\ & \times [E_\nu - (M_n - M_p)c^2] \\ & \times \{ [E_\nu - (M_n - M_p)c^2]^2 - (m_e c^2)^2 \}^{1/2} .\end{aligned} \tag{8}$$

The transition matrix element has been expressed in terms of the free neutron decay ft value, where the phase-space factor $f = 1.714\,65 \pm 0.000\,15$ follows from calculation[21] and $t_{1/2} = 622 \pm 11$ sec is the neutron half-life taken as the average over experimentally determined values.[22] We take into account the two correction terms (both of 1% order of magnitude).

(i) Correction for weak magnetism[23] arising from the difference in the anomalous magnetic moments of the neutron and the proton, $\mu = \mu_n - \mu_p = 3.71$ nuclear magnetons,

$$\delta_{\rm WM}(E_{e^+}) = -2\frac{\mu\lambda}{1+3\lambda^2}[E_{e^+} + (M_n - M_p + m_e)c^2 + \beta p_{e^+}]/M , \tag{9}$$

where

$$\lambda = g_A / g_V = 1.26 \tag{10}$$

is the ratio of axial-vector and vector coupling constants.[22]

(ii) Radiative corrections[23] of order α, including the contribution of internal bremsstrahlung

$$\delta_{\rm rad}(E_{e^+}) = 11.7 \times 10^{-3} E_{e^+}^{-0.3} \tag{11}$$

with the positron kinetic energy E_{e^+} in MeV.

Corrections to Eq. (8) due to finite nucleon mass lead to slight changes of the e^+ spectrum ($< 2 \times 10^{-3}$) (Ref. 23), and were neglected. In summary, we arrive at the cross section

$$\begin{aligned}\sigma(E_\nu) = {} & (9.43 \pm 0.17)(E_\nu - 1.293) \\ & \times [(E_\nu - 1.293)^2 - 0.511^2]^{1/2} \\ & \times (1 + \delta_{\rm WM} + \delta_{\rm rad}) 10^{-44} \text{ cm}^2 ,\end{aligned} \tag{12}$$

where E_ν is the neutrino energy in MeV and $E_{e^+} = E_\nu - 1.804$ MeV.

IV. THE NEUTRINO DETECTION SYSTEM

The neutrino detector is nearly identical to the one previously used for the measurements at the ILL reactor,[11] but with the additional feature of position sensitivity. The central detector unit is approximately one cubic meter in size and consists of two systems of counters, which record, respectively, the positron and neutron generated in the detection reaction $\bar{\nu}_e + p \rightarrow e^+ + n$ as shown in Fig. 3. Thirty cells, filled with a proton-rich liquid scintillator and arranged in five planes served both as target for the incident antineutrinos and as detector for the generated

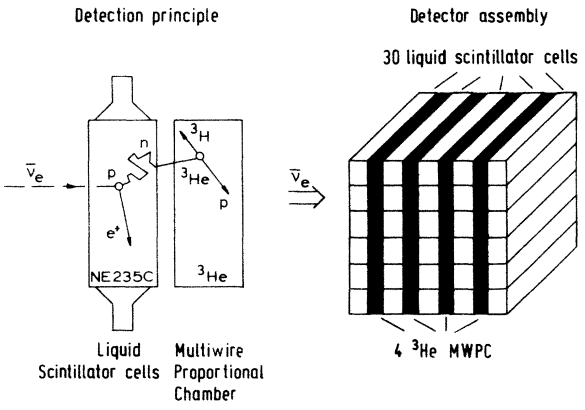

FIG. 3. Neutrino-detection principle and realization: The central neutrino-detector unit consists of 30 liquid-scintillator cells arranged in five planes for positron detection and four ^{3}He-filled wire chambers for neutron detection.

positrons. The reaction neutrons emerging with an energy of several keV are thermalized in the scintillator cell within a few μ sec and diffuse within a mean diffusion time of about 150 μ sec into one of the adjacent wire chambers filled with ^{3}He, where they are detected. A valid neutrino event requires as signature a proper spatial correlation as well as a coincidence within a time window of 250 μ sec between a positron in a scintillator cell and a neutron in one of the wire chambers.

A. Positron detection

The target cell contained a total of 377 l of liquid scintillator (Nuclear Enterprise NE235C, H/C=1.700 $\pm$0.015, ρ=0.858$\pm$0.005 g/cm^3) providing a proton density of (6.39$\pm$0.07)$\times 10^{22}$ cm^{-3} and pulse-shape-discrimination (PSD) capability. To optimize light collection and energy resolution the liquid scintillator (transmission length $\geq$3 m) was contained in 30 Lucite cells each with external dimensions of 88$\times$20$\times$9 cm^3. The individual cells were equipped on both ends with two photomultipliers (AMPEREX XP2312) coupled together. The event position along the length of a scintillator cell was determined from the time difference between the photomultiplier signals at both ends with a spatial resolution of about 6 cm. Spatial resolution in the other two directions was limited by the height and width (20$\times$9 cm) of the cell.

The target cell energy resolution was 18% full width at half maximum (FWHM) at 0.91 MeV as measured with forwardly scattered Compton electrons produced in the scintillator with a ^{65}Zn single-γ-ray source.[11] The energy response of a cell varied by less than 5% between the center of the cell and either end where the photomultipliers are mounted. This variation was taken into account when establishing the absolute energy calibration.

For the energy calibration the Compton edge of the 4.44-MeV γ rays in ^{12}C* from an Am-Be neutron source (4.20 MeV) and the 2.22-MeV γ ray from neutron capture by protons (2.03 MeV) was used. The error in the calibration, mainly due to the unfolding of the Compton edges, was 1.2%. The linearity of the system could be checked by using the measurements at 0 MeV (pedestal), and at the above-mentioned Compton edges of 0.91, 2.03, and 4.20 MeV.

The energy response function of the detector to positrons with a given energy and spatial distribution inside a cell was calculated by Monte Carlo simulation. Several effects were included.

Escape effects. The average energy deposited by a positron inside the target cell was determined by integrating the specific energy loss dE/dx over the total traversed path. An energy straggling according to a Landau distribution was included. This effect caused a low-energy tail in the response function for monoenergetic positrons, reflecting the energy loss by escape.

Positron annihilation. Annihilation at rest gives rise to two 511-keV γ rays (attenuation length 12 cm in the scintillator), which deposit little energy in the cell and distort the upper flank of the positron peak. If the positrons annihilate in flight, part of their kinetic energy is lost to annihilation γ rays and consequently intensity is added only to the low-energy tail of the response function.

Bremsstrahlung. Positron bremsstrahlung causes the transfer of intensity from the high-energy to the low-energy side of the response function.

Wall corrections. The 6.35-mm-thick Lucite walls of each scintillator cell also act as neutrino targets (Lucite: $C_5H_8O_2$, density ρ=1.18 g/cm^3, H/C=1.6). Positrons created in the Lucite and entering the scintillator contribute intensity at the low-energy tail of the response function.

The final positron response function $r(E_{e+},E'_{e+})$ of the

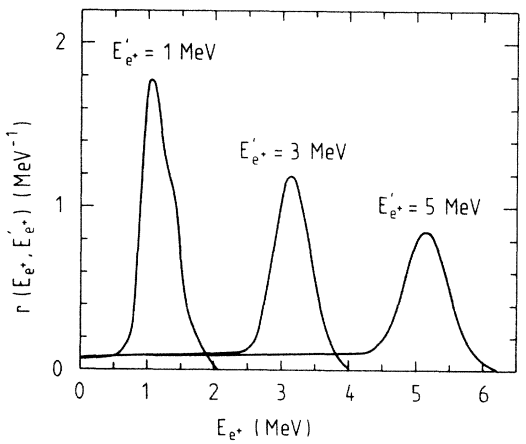

FIG. 4. Positron response functions $r(E_{e+},E'_{e+})$ of the scintillator cells for three initial positron energies E_{e+} (1, 3, 5 MeV) as a function of the deposited energy E'_{e+} observed in the scintillator cell. The curves are the results of Monte Carlo simulations smeared out with the energy resolution of the scintillator cells. In the normalization of the resolution function the effect of Lucite was taken into account.

scintillator cells for three initial positron energies E_{e+} is illustrated in Fig. 4 as a function of the deposited energy E'_{e+} observed in the scintillator cell.

B. Neutron detection

Multiwire proportional chambers filled with a gas composition of 95% (volume) ^{3}He and 5% (volume) CO_2 are practically black absorbers for thermal neutrons (capture cross section 5500b). The capture reaction $n + {}^3\text{He} \rightarrow p + t$ has a Q value of 765 keV. Since a neutron event in one of the wire chambers was used as the detection trigger, great care was taken to minimize any excess counting rate, arising, for example, from natural radioactivity in the construction materials. All chamber materials were chosen for low α-background activity. Only stainless steel (VA4301), copper, and Teflon were used as construction materials. Solder was covered by Teflon sheets. To minimize neutron capture in the chamber walls, 0.4-mm-thick steel foils without any enforcement were chosen, necessitating counter operation at atmospheric pressure. Under these operating conditions the ionization tracks of the reaction products extend over a region of roughly 5 cm.

Each wire chamber consists of two main components: the proper stainless-steel chamber box ($126 \times 97.3 \times 8$ cm^3) with its walls acting as cathode planes and an anode wire frame, which is rigidly mounted onto the front flange (Fig. 5). To avoid any surface irregularities, which might have caused local discharges, all stainless-steel parts were mechanically or electrolytically polished. After careful cleaning and baking of all detector components the chambers were permanently sealed. There was no observable degradation of the counting performance after four years of continuous operation. The energy resolution of the wire chambers was significantly influenced by inhomogeneous field configurations inside the chamber. In particular, the large and unsupported cathode planes of the counters were not perfectly flat, degrading the energy resolution. Off-line correction for field inhomogeneities became possible by taking advantage of the position sensitivity of the counters to establish a "gain map" used to compensate for the position-dependent energy gain. The overall energy resolution of the neutron counter was thereby substantially improved. A typical spectrum is shown in Fig. 6. In the off-line data analysis position sensitivity allowed the masking off of a few local regions (some 5% of the detector volume) which had elevated counting rates due to local discharges.

Position sensitivity along the anode wires was obtained by charge division. The wire plane consists of 64 resistive (1.2 kΩ/m) 25-μm-diameter CrNi wires with wire spacing of 1.7 cm, allowing subdivision of the anode plane into 16 stripes of four wires each. Every stripe is connected to the next but one neighbor in the back of the chamber via a 47-Ω resistor. This arrangement was necessary to avoid ambiguities, since proton-triton events could extend over two adjacent stripes. In case an event induces pulses on two adjacent stripes, the horizontal position is evaluated for that stripe which carries the higher charge. By comparing the sum of the pulse heights from both stripes it is possible to interpolate the vertical position between stripes (Fig. 7). The individual stripes are separately biased with a high voltage of 2.4 kV and capacitively (10 nF) coupled

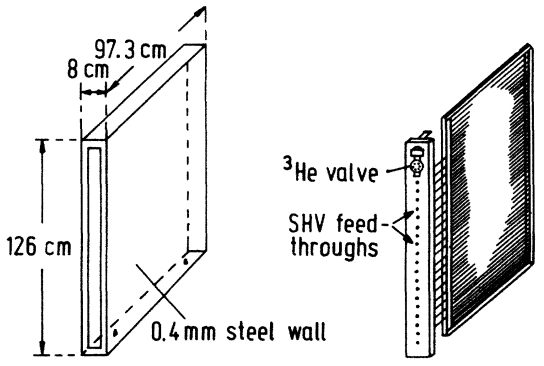

FIG. 5. Arrangement of the ^{3}He position-sensitive multiwire chamber. The wire plane (right) is rigidly mounted to the front flange of the chamber box (left).

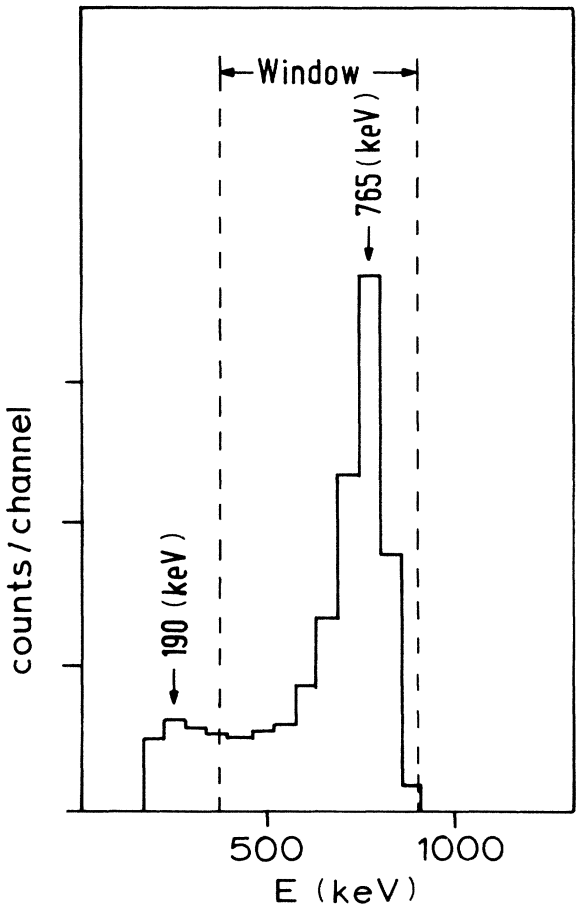

FIG. 6. Energy spectrum of a wire chamber following n capture on ^{3}He. The spectrum is corrected for gain variations within the chamber. The employed pulse-height window (acceptance 0.834±0.003) is indicated by the dashed lines.

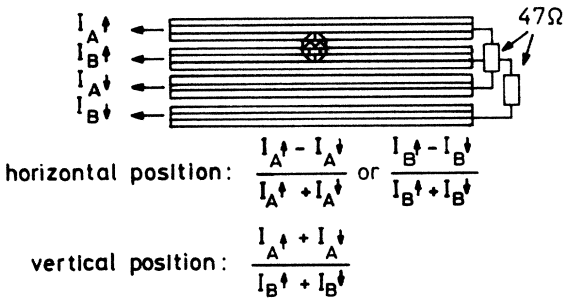

FIG. 7. Layout of wire-chamber stripe system: The vertical position of an event is obtained by comparing the charges induced on neighboring stripes. The horizontal position of an event is obtained by charge division along the stripe carrying the higher charge.

to a current-sensitive preamplifier.

The detection efficiency of the wire chamber was measured with a Sb-Be source of known neutron activity (calibration error 1%). The energy spectrum of the emitted 25-keV neutrons closely matches the spectrum of the neutrons generated in a neutrino interaction. For calibration purposes, the source was mounted inside a replacement scintillator cell with the same dimensions as the detector cells. This calibration cell was filled with the same liquid scintillator and substituted for certain scintillator cells in key positions within the detector. The neutron source position within the cell was selected with stepping motors in the x, y, and z direction. About 60 calibration points (statistical error 1.5%) were recorded along the width, the height, and one-half of the length of a cell. The efficiency at a specific coordinate in the cell was obtained by comparing the number of neutrons emitted by the source in the cell to those measured in the adjacent wire chambers. The total neutron detection efficiency was obtained by integrating the position-dependent efficiency over the volume of a cell and by averaging over all cell positions in the detector. This procedure gave a neutron efficiency value of $\epsilon_n = 0.217 \pm 0.008$ (68% C.L.) for our particular pulse-height window acceptance of 0.834 ± 0.003 (Ref. 24).

C. Background suppression

Radiation from the reactor and cosmic radiation are the two potential external background sources for the neutrino detector. Differential shielding tests performed in a previous experiment at the ILL reactor demonstrated that the shielding at that site was sufficient to eliminate any reactor associated background. Shielding conditions for the experiments at Gösgen were superior since the neutrino detector was always located outside of the reactor containment building which alone furnished already 8 m of concrete shielding towards the core. In addition the uncorrelated singles rates in the scintillator cells and in the neutron wire chambers did not change for reactor on and off. Thus any reactor associated background could safely be assumed to be negligible.

The attenuation of the hard nucleonic component of the cosmic radiation is achieved by heavy shielding. This shielding unfortunately introduces additional background sources due to ^{40}K activity in the concrete and due to secondary neutron production caused by muon and hadron interactions within the shielding material. The neutrino detector is completely surrounded (starting from the outside) by several shielding layers (Fig. 8): 2 m of concrete with an additional 2 m of concrete on top, 15 cm of iron (to suppress ^{40}K activity), 20 cm of water contained in steel tanks of 8 mm wall thickness (to thermalize and absorb neutrons), and 5 mm plates of B_4C loaded plastic (to absorb slow neutrons).

Fast neutrons created by cosmic-ray muons in the surrounding material can initiate a proton recoil in a scintillator cell and subsequently thermalize and diffuse into a wire chamber. With the recoiling proton causing ionizations in the scintillator cell and with the associated neutron triggering a wire chamber a signal identical to a valid neutrino event would normally appear. Pulse-shape discrimination (PSD) is therefore applied to the pulses from the scintillator cells to distinguish proton recoils from genuine positron events. The effectiveness of this discrimination is illustrated in Fig. 9. The PSD technique reduces the background caused by muon-induced fast neutron events by about a factor of 10. The slight overlap of the positron and neutron peaks in the PSD spectra requires the fast neutron flux at the detector site be not much higher than the expected neutrino event rate (several counts per hour).

The highly penetrating muonic component of the cosmic radiation cannot be significantly reduced by means of shielding. Muons may produce, via collision or capture processes, additional background by generating secondary neutrons in the matter surrounding the detector. To reject these muon-induced events, an active veto system has been installed, consisting of six 12-cm-thick liquid-scintillator-filled panels completely surrounding the central detector unit.[11] A muon traversing the active veto system gen-

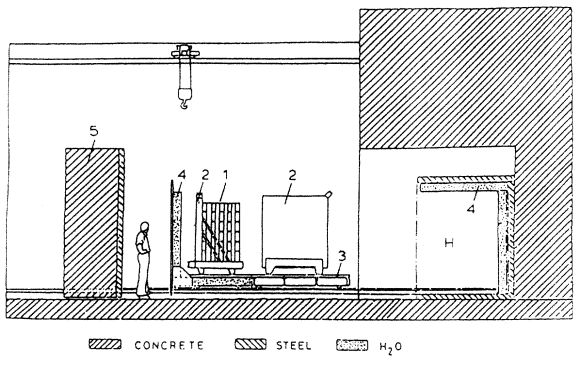

FIG. 8. Detector assembly of the neutrino experiments I–III at Gösgen. The central detector, normally located within the concrete house H is shown in its rolled out position. (1) is the central detector unit, (2) are the tanks of the active veto, (4) are water tanks, (5) is a movable concrete closing door. The various parts of the detector move on a system of rails (3).

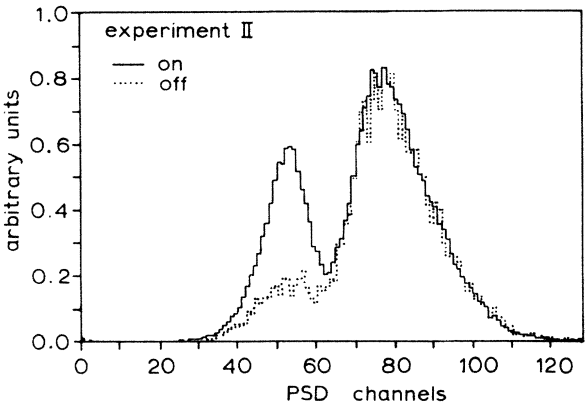

FIG. 9. Example of a PSD spectrum obtained in the position of experiment II for reactor-on data (solid curve) and reactor-off data (dashed curve). The channel number is proportional to the decay time of the light pulse associated with the recoiling particle. For reactor-on data the peak on the left is enhanced due to neutrino-induced positrons (0.7 MeV $< E_{e^+} <$ 5.6 MeV), while the neutron peak on the right remains unchanged.

erates 10- and 320-μsec-long gate pulses. The shorter gate pulse serves to reject scintillator cell pulses associated with these muons. The longer gate pulse is used to reject muon-generated neutrons that appear within this time window in one of the wire chambers, after thermalization in the material surrounding the detector. Both these types of events are rejected in the off-line analysis. The total average counting rate in the six veto scintillators amounted to 260, 300, and 340 sec^{-1} for experiments I—III. The unvetoed singles rate of the shielded scintillator cells was $\approx$300 sec^{-1} above a threshold of 0.7 MeV, more than half of which was due to ^{40}K radioactivity in the photomultipliers.

D. Detector control

The detector was calibrated every four days. For this purpose two Am-Be neutron sources were mounted near the front and back veto panels, facing each other. Energy and position spectra were recorded for each of the 64 anode stripes of the wire chambers and compared with nominal spectra. Within a period of 4 days between calibrations only very small shifts occurred which were corrected by gain adjustments. The energy calibration stability of the scintillator cells was controlled with the Compton edges at 2.03 and 4.20 MeV produced by Am-Be neutron sources (Sec. IV A). Also the zero-energy point (pedestal) was carefully checked every 4 days. Only small drifts ($<1\%$) in gain of a few cells in both directions could be observed thus resulting in a negligible net shift of the cell ensemble over periods of 4 days. The scintillator cell gains were corrected for by changing the high voltage of the photomultipliers. In a separate calibration measurement the scintillator cells were checked by measuring cosmic-ray produced position and PSD spectra. Care was taken to maintain constant operating conditions for the detector and for the electronic setup over the entire measuring period of 4 years. Heat produced inside the veto house was removed by a constant flow of cooling water. The temperature of the detector was stabilized to ± 0.5 °C during all measurements. Moreover the temperature inside the electronics trailer was kept constant to within ± 1 °C.

V. DATA ACQUISITION AND DATA PROCESSING

A. Data acquisition

Upon receiving a trigger from one of the wire chambers above the hardware threshold of 100 keV (total rate 1.2 sec^{-1}), the event data are read via CAMAC into a PDP 11/34. The event data consist of the energy, position, and time of the wire chamber event, of the veto counter flags, and of energy, position, PSD, and time information of the three previous events in the scintillator cell assembly. The subsequent on-line analysis uses these data to construct preliminary spectra and to update software and hardware scalers. This analysis is used to monitor the performance and stability of individual detector components. Events for which the triggering wire-chamber pulse lies above a software threshold of 150 keV are subsequently written on tape. Recording simultaneously data from three preceding scintillator cell events allows an on-line measurement of the accidental background, which essentially arises from ^{40}K radioactivity in the photomultipliers and cosmic-ray muon events. The correlated background is measured during the reactor-off periods. Table II summarizes the time schedule for the experiments I—III, as well as the duration of the actual data taking. The table also shows the system live-time fractions, which are determined by a pulser measurement. In going to larger distances L these live-time fractions decrease, since the cosmic-ray-generated veto rates and thereby dead time increase, when moving away from the shadow of the reactor containment building.

B. Data reduction

The first step in the off-line analysis consists of preparing the data of individual tapes to be added together. Thus, where necessary, the position spectra of both counter systems were shifted by small amounts to match them to the nominal position spectra. The position-dependent energy gain in the wire chambers was compensated for by making use of a previously established "gain map." Similarly the energy dependence of the PSD response was removed by adjustment of the PSD pulse height such that the center of the upper slope of the γ-ray—positron line coincides for all energies. The energy-dependent shift parameters were determined previously using accidental and cosmic events.

In a second step, several selection criteria are imposed on the data in order to extract neutrino-induced events. For a good event the following conditions are required.

(a) The neutron event is not coincident with a long (320-μsec) veto signal.

(b) The neutron trigger originates from a single or from two adjacent stripes of one wire chamber.

(c) The wire-chamber pulse height should fall within a

TABLE II. Time schedule and signal rates for experiments I–III. The live-time fraction for the three experiments are also shown.

Experiment	ν data taking	Background	Number of neutrino events	Live-time fraction
I (37.9 m)	August 1981—January 1982 (real time: 3440.54 h)	June 1981—July 1981 (real time: 551.16 h)	10909±220	0.835±0.004
II (45.9 m)	July 1982—May 1983 (real time: 4894.67 h)	June—July 1982 and June—July 1983 (real time: 1727.77 h)	10605±190	0.833±0.003
III (64.7 m)	October 1983—May 1984 July 1984—May 1985 (real time: 8608.47 h)	June 1984 and June—July 1985 (real time: 1457.66 h)	8787±325	0.829±0.003

preselected window.

(d) The scintillator cell event is not in coincidence with a short (10-μsec) veto signal.

(e) The data from the last recorded scintillator cell event prior to the trigger signal is observed only in one cell which must be adjacent to the triggering wire chamber.

(f) The last scintillator cell event is not preceded within 250 μsec by any second scintillator cell event. This avoids selecting a wrong positron event.

This first set of selection criteria reduces the primary data rate by a factor of 30. In addition we impose further requirements.

(i) PSD condition. The pulse from the scintillator cell must fall within the window set for positrons in the PSD spectrum.

(ii) Time characteristic. Figure 10 shows the distribution of time intervals between a positron and a neutron event. As indicated in the figure, the correlated event is required to fall within a time window of 250 μsec which has an acceptance of $\approx 88\%$.

(iii) Position correlation. Figure 11 shows along the length (right) and height (left) of a wire chamber the distribution of the projected distances of neutrino-induced correlated events in a scintillator cell and a wire chamber. About 90% of neutrino-induced events are retained in the 24-cm-wide position window. Simultaneously the accidental counting rate is reduced by a factor of 6.25.

Taking into account that the slow-neutron calibration was performed during experiment I, we write the total energy-independent efficiency ϵ^j $(j=1,2,3)$ for neutrino-induced correlated events as

$$\epsilon^j=\epsilon_n(\epsilon_W^j/\epsilon_W^1)\epsilon_m^j\epsilon_p^j\epsilon_t^j ,$$

where ϵ_n is the slow neutron detection efficiency described in Sec. IV B, ϵ_W^j is the wire-chamber pulse-height window acceptance as determined with fast neutron background, ϵ_m^j originates from the masking off of small discharge areas in the wire chambers (Sec. IV B), ϵ_p^j is the position acceptance window, confining the projected distances between correlated positron and neutron events to a maximum of 24 cm, and ϵ_t^j takes into account the chosen 250-μsec time window for correlated events. Table III

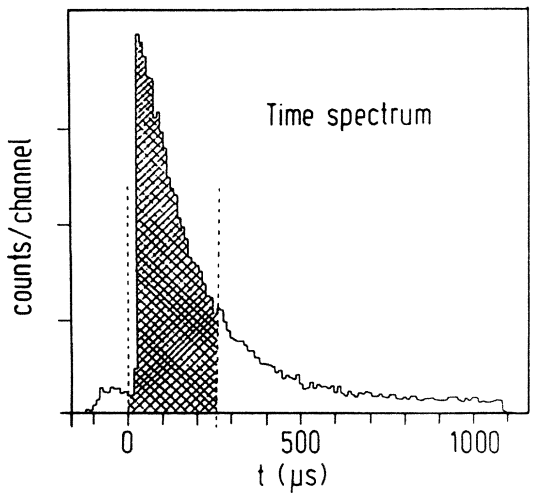

FIG. 10. Distribution of time intervals between neutrino-induced events in a scintillator cell and a wire chamber. The shaded area corresponds to the employed time window of 250 μsec.

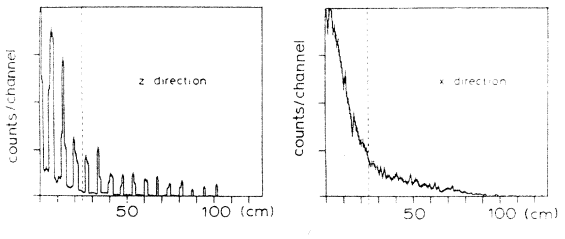

FIG. 11. The distribution of distances between neutrino-induced correlated events in a scintillator cell and a wire chamber projected along the length (right) and height (left) of a chamber. The comblike pattern (in the vertical direction) is due to the discrete arrangement of the horizontal scintillator cells and the wire groups. A position window of 24 cm is employed.

TABLE III. Summary of the energy-independent efficiencies resulting from the various selection criteria. The stated errors are 68% C.L. The value of ϵ_W from experiment I is included in ϵ_n.

	Expt. I (37.9 m)	Expt. II (45.9 m)	Expt. III (64.7 m)
Slow neutron (ϵ_n)		0.217±0.008	
Wire-chamber pulse height (ϵ_W)	0.834±0.003	0.828±0.002	0.842±0.002
Wire-chamber position mask (ϵ_m)	0.969±0.004	0.963±0.004	0.963±0.004
Wire-chamber position cut (ϵ_p)	0.900±0.012	0.908±0.012	0.904±0.012
Neutron-positron time window (ϵ_t)	0.879±0.003	0.879±0.003	0.879±0.003
Total energy-independent efficiency (ϵ^j, $j=1,2,3$)	0.167±0.006	0.165±0.006	0.168±0.006

gives these efficiencies, together with their 68% C.L. errors for experiments I–III. The individual efficiency values demonstrate that within the stated errors the system remained stable throughout the entire measuring period. The energy-independent efficiencies ϵ^j discussed so far must still be multiplied by one energy-dependent efficiency function, the PSD acceptance $a^j_{\rm PSD}(E_{e+})$. The PSD relies on the specific energy loss of the particles in the scintillator cell and therefore becomes a function of energy. A separate determination of the PSD acceptance $a^j_{\rm PSD}(E_{e+})$ was performed for experiments I–III using the accidental background. Such an event sample is practically free of neutrons and only contributes to the peak on the left of Fig. 9, where the positron events are located. This allows us to continuously determine the energy-dependent tail of the positron peak under the neutron peak. Throughout each of the experiments I–III the PSD acceptances remained stable to better than 1%.

VI. DATA ANALYSIS AND RESULTS

A. Measured positron spectra

Table II shows for experiments I–III the total number of neutrino-induced events within the energy interval of 0.7 MeV $< E_{e+} <$ 5.6 MeV. The measured spectra (reactor on, reactor off) are shown in Fig. 12(a) together with the respective accidental backgrounds. The resulting positron spectra (reactor on minus reactor off) $Y^j_{\rm expt}(E_{e+})$ are presented in Fig. 12(b) and listed separately in Table IV (the bin width of 0.305 keV is roughly adapted to the energy resolution).

B. Predicted positron spectra

The expected positron yield $Y^j(E_{e+},L^j,\Delta m^2,\theta)$ per MeV and hour for a mean neutrino source-detector distance L^j is given by

$$Y^j(E_{e+},L^j,\Delta m^2,\theta)=[4\pi(L^j)^2]^{-1}n_p\epsilon^j a^j_{\rm PSD}(E_{e+})\int\int\delta(E'_\nu)\sigma(E'_\nu)\eta^j(E'_\nu)S(E'_\nu)P(E'_\nu,L',\Delta m^2,\theta)\times r(E_{e+},E'_{e+})h(L',L^j)dL'dE'_{e+}\ , \tag{13}$$

where $E_{e+}=E_\nu-1.804$ MeV, n_p is the total number of target protons in the scintillator, ϵ_j is the energy-independent detection efficiency (Sec. V B), $a^j_{\rm PSD}(E_{e+})$ is the PSD acceptance (Sec. V B), and $\delta(E_\nu)$ is a function which corrects for the shifts in the energy scale caused when recoil effects, due to the finite proton mass, are taken into account. This correction can be parametrized as

$$\delta(E_\nu)=1-0.155\exp[(E_\nu-8)/1.4]\ ,$$

with E_ν in (MeV). $\sigma(E_\nu)$ is the detection reaction cross section (Sec. III B), $\eta(E_\nu)$ is a factor correcting for slight differences in reactor fuel compositions for experiments I–III as illustrated in Fig. 2, $S(E_\nu)$ is the neutrino source spectrum, $P(E_\nu,L^j,\Delta m^2,\theta)$ is the two-neutrino-

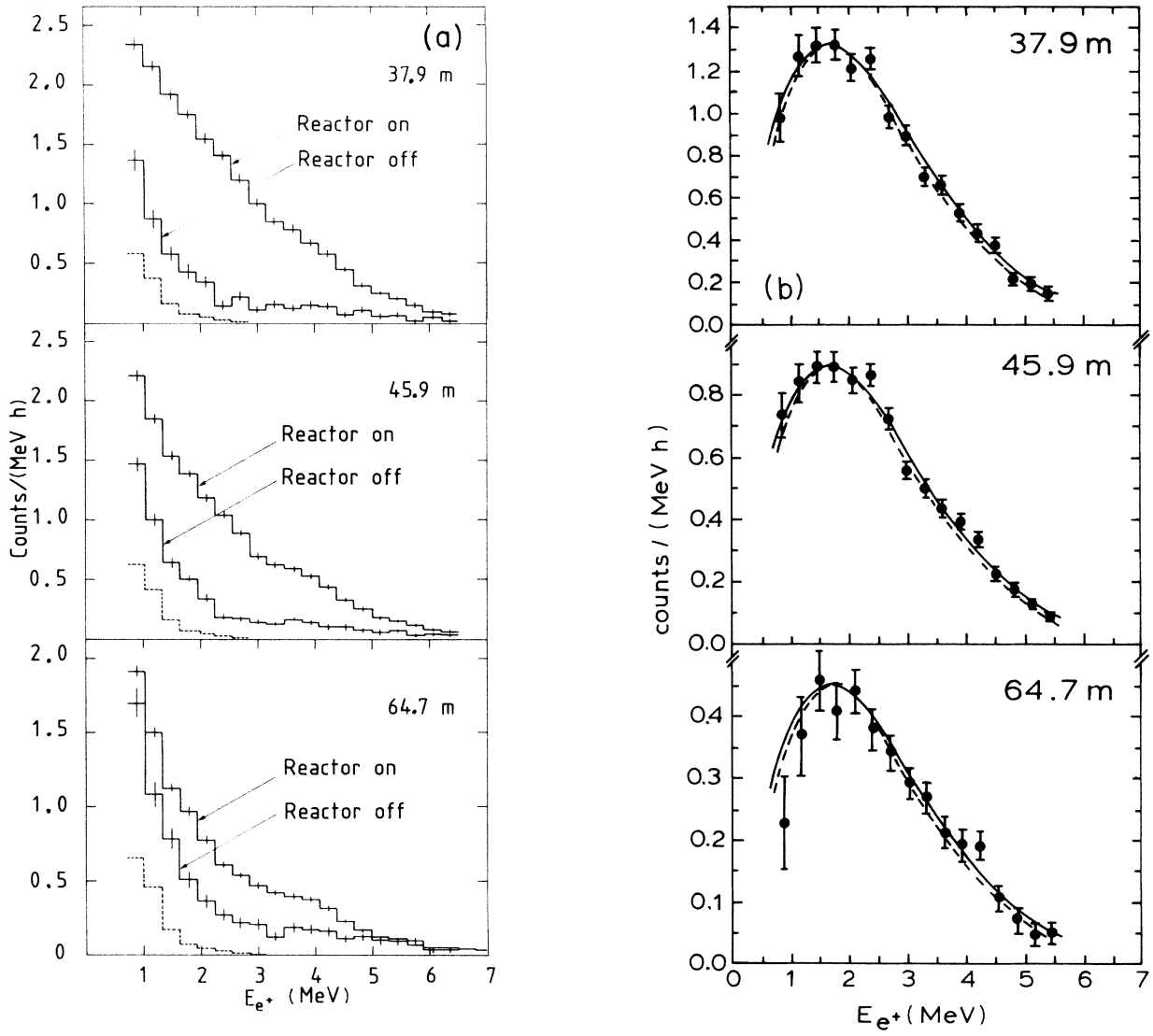

FIG. 12. (a) Experimental spectra for reactor-on and reactor-off periods after application of all selection criteria. Bin width 0.305 MeV. The errors shown are statistical. The contributions of the accidental background are indicated by the dashed curves. (b) Measured and predicted positron yields. The measured positron spectra obtained from the subtraction of reactor-on and reactor-off spectra are shown for experiments I—III. The errors shown are statistical. The solid curves represent the predicted positron yields derived by using the (fitted) reactor antineutrino spectrum $S_A(E_\nu)$ for the case of no oscillations and therefore is based exclusively upon data from our experiments I—III. The dashed curves represent the predicted positron yields derived by using the spectrum $S_B(E_\nu)$ based on independent β-spectroscopic data.

oscillation function given by Eq. (5), $r(E_{e^+},E'_{e^+})$ is the energy response function of the detector (Sec. IV A), and $h(L',L^j)$ is a spatial distribution function, which accounts for the spread of the distances L^j due to the geometrical extent of the reactor core and the neutrino detector. This function was determined by Monte Carlo simulation.

Using the reactor antineutrino spectrum $S_B(E_\nu)$ of Eq. (7) and assuming the absence of neutrino oscillations we obtain from Eq. (13) the predicted positron yields shown in Table IV. Table V lists separately for experiments I—III the ratios of the integrated experimental positron yield to the corresponding integrated yield predicted for no oscillations. The systematic errors of the three ratios are highly correlated and arise essentially from uncertainties in the absolute normalization of the reactor antineutrino spectrum (3.0%, 68% C.L.), the cross section (2%, 68% C.L.) the detection efficiency (3.8%, 68% C.L.), and the reactor power (2%, 68% C.L.). Together with a few more error sources of $<1\%$ each, we obtain by quadratic addition a correlated systematic error of 6%. The individual systematic errors reflect detector instabilities of 1%

TABLE IV. Experimental positron spectra $Y^j_{\text{expt}}(E_{e+})$ and the predicted positron spectra for no oscillations; $Y^j_0(E_{e+})=Y_B(E_{e+},L^j,\Delta m^2=0,\sin^2 2\theta=0)$. The spectra are given in units of counts/MeV h.

Energy E_{e+} (MeV)	$Y^1_{\text{expt}}(E_{e+})$ (MeV^{-1} h^{-1})	$Y^1_0(E_{e+})$	$Y^2_{\text{expt}}(E_{e+})$ (MeV^{-1} h^{-1})	$Y^2_0(E_{e+})$	$Y^3_{\text{expt}}(E_{e+})$ (MeV^{-1} h^{-1})	$Y^3_0(E_{e+})$
0.877	0.975(113)	0.970	0.734(72)	0.657	0.227(75)	0.334
1.182	1.268(94)	1.175	0.837(62)	0.792	0.367(63)	0.402
1.487	1.319(80)	1.302	0.887(52)	0.876	0.457(50)	0.443
1.792	1.323(71)	1.328	0.882(48)	0.893	0.407(45)	0.452
2.097	1.212(65)	1.281	0.843(42)	0.862	0.439(36)	0.435
2.402	1.256(52)	1.179	0.861(36)	0.793	0.378(35)	0.399
2.707	0.979(54)	1.020	0.721(33)	0.685	0.340(28)	0.345
3.012	0.890(44)	0.867	0.555(30)	0.581	0.291(26)	0.292
3.317	0.695(46)	0.744	0.496(28)	0.497	0.267(24)	0.249
3.622	0.657(43)	0.617	0.433(29)	0.413	0.212(25)	0.207
3.927	0.524(43)	0.509	0.391(27)	0.340	0.191(26)	0.171
4.232	0.430(41)	0.406	0.332(24)	0.270	0.190(23)	0.136
4.537	0.374(32)	0.307	0.223(22)	0.204	0.105(21)	0.102
4.842	0.212(33)	0.239	0.175(20)	0.159	0.069(19)	0.079
5.147	0.191(26)	0.174	0.125(16)	0.115	0.047(18)	0.058
5.452	0.144(26)	0.110	0.087(16)	0.073	0.050(15)	0.037

(68% C.L.). Because of the poor signal-to-background ratio these instabilities play an increasing role for larger distances and therefore the individual normalization error is biggest in the 64.7-m position. In addition, we have uncertainties in the reactor powers for the individual experiments of about 1%. The errors are summarized in Table V.

C. Data analysis

There are two principally different approaches for analyzing the results of the experiments. Analysis A relies solely on a comparison of measurements taken at three distances from the core of the Gösgen reactor. We thereby arrive at limits on the oscillation parameters which are practically decoupled from uncertainties in the reactor antineutrino spectrum at $L=0$, the detector efficiency, and the reaction cross section. Analysis B uses in addition to the measured spectra at three distances the predicted positron spectrum as given in Table IV. Inclusion of these data increases the sensitivity to oscillation parameters as compared to analysis A, particularly for the case of large Δm^2.

Analysis A. Only slight relative changes of reactor burn up conditions and detector efficiencies enter into this analysis. Absolute values of the detector efficiency, the detection cross section, and the reactor antineutrino spectrum essentially cancel. The result of this analysis can be regarded as free from all external assumptions and is the safest limit which can be given for the oscillation parameters.

In order to test the compatibility of a certain oscillation hypothesis $(\Delta m^2,\theta)$ with the measurements I–III, the following χ^2 expression was defined:

$$\chi^2(\Delta m^2,\theta)=\sum_j\sum_k\left[\frac{Y^j_{\text{expt}}(E_k)-N^j Y^j{}_A(E_k,L^j,\Delta m^2,\theta)}{\sigma_{j,k}}\right]^2+\sum_j\left[\frac{N^j-1}{\sigma_j}\right]^2, \tag{14}$$

where $Y^j_{\text{expt}}(E_k)$ are the positron yields measured at distances L^j $(j=1,2,3)$ with $\sigma_{j,k}$ being the associated statistical uncertainties. The mean energy of a bin is given by E_k $(k=1,\ldots,16)$. The positron yields $Y^j_A(E_k,L^j,\Delta m^2,\theta)$ follow from Eq. (13) by introducing the reactor antineutrino spectrum $S(E_\nu)$ in the following parametrized form:

$$S_A(E_\nu)=\exp\left[\sum_l A_l E_\nu{}^l\right], \tag{15}$$

where S_A is in units of 10^{19} MeV^{-1}sec^{-1} and E_ν is in

TABLE V. Ratios of experimental positron yield to that predicted for no oscillations for experiments I–III. Errors are 68% C.L.

Experiment	Ratio	Statistical error	Individual uncorrelated systematic error	Common correlated systematic error
I (37.9 m)	1.018	±0.019	±0.015	±0.060
II (45.9 m)	1.045	±0.019	±0.015	±0.060
III (64.7 m)	0.975	±0.036	±0.030	±0.060

MeV. Such a representation suggests itself, since the neutrino spectra per fission do not exhibit significant structures beyond the point-to-point errors. The parameters N^j ($j=1,2,3$) are respective normalizations with associated uncertainties σ_j. The variations in these parameters result from the uncorrelated individual systematic errors in the predicted yields Y_A^j for experiments I–III (fourth column in Table V) which are on the percent level. The introduction of these respective normalizations gives rise to the last sum in Eq. (14). The expression for χ^2 thus contains experimental uncertainties for 16 energy bins, taken at three positions L^j each, i.e., 48 values for $\sigma_{j,k}$, together with three additional values σ_j, yielding altogether 51 variances. The expression for χ^2 is minimized for fixed values of Δm^2 and θ, by varying the six parameters N^j and A_l. One thereby fits the results of experiments I–III by one common reactor antineutrino spectrum. It turns out that three parameters A_l ($l=0,1,2$) are sufficient to describe the reactor antineutrino spectrum and that the addition of a fourth parameter does not change the result. Thus the minimization procedure leads to 45 degrees of freedom. The resulting value for the no oscillation case is $\chi^2(0,0)=41.1$, with the parameters $A_0=3.80$, $A_1=-0.571$, $A_2=-0.044$. The three fitted positron spectra $Y_A^j(E_{e^+},L^j,\Delta m^2=0,\theta=0)$ are shown in Fig. 12(b) by solid lines. The minimum value for χ^2, $\chi^2_{\min}=38.8$, is found for the parameter set $(\Delta m^2)^*=0.87$ eV^2, $(\sin^2 2\theta)^*=0.10$, $(A_0)^*=3.85$, $(A_1)^*=-0.572$, and $(A_2)^*=-0.044$.

To test a particular oscillation hypothesis $(\Delta m^2,\theta)$ against the parameters of the best fit we compute the logarithm of the ratio of the likelihood functions for the two cases:[25]

$$\lambda(\Delta m^2,\theta)=\tfrac{1}{2}[\chi^2(\Delta m^2,\theta)-\chi^2_{\min}] \ . \tag{16}$$

Clearly a small λ value means that the hypothesis is in good agreement with the data, a large one means that it is not. To be more quantitative the expected distribution of λ was calculated by Monte Carlo simulations. In this simulation we assume a distinct oscillation hypothesis $(\Delta m^{2\prime\prime},\theta'')$ and simulate a great number of experimental positron spectra by scattering the individual data points around the predicted positron yields $Y_B(E_{e^+},L^j,\Delta m^{2\prime\prime},\theta'')$, with the Gaussian-assumed variances given by $\sigma_{j,k}$. For each of these simulated data the quantity

$$\lambda(\Delta m^{2\prime\prime},\theta'')=\tfrac{1}{2}[\chi^2(\Delta m^{2\prime\prime},\theta'')-\chi^2_{\min}]$$

is determined, the distribution of which is representative of the scattering of χ^2_m around the "true" value $\chi^2(\Delta m^{2\prime\prime},\theta'')$. This simulation was done for several sets of parameters $(\Delta m^{2\prime\prime},\theta''$ in the relevant range yielding practically each time the same λ distribution. It was thus possible to adopt a unique distribution for the λ values. Comparing then the value $\lambda(\Delta m^2,\theta)$ determined for the real measured data with this expected λ distribution one can assign a degree of confidence to the oscillation hypothesis $(\Delta m^2,\theta)$. The no-oscillation hypothesis with $\chi^2(0,0)=41.1$ (45 degrees of freedom) is found to be in excellent agreement with the data. The region in the Δm^2 vs $\sin^2 2\theta$ plane allowed by our data at the 68% (dashed curve) and 90% (solid curve) confidence is shown in Fig. 13(a). All parameters lying to the right of the curves are excluded by our experiment with the indicated confidence level, while the parameter regions to the left of the curves are still compatible with our data. Instead of using the parametrized spectrum of Eq. (15), which relies on the smoothness of the reactor antineutrino spectrum, we have also performed a different analysis still relying only on our measured data. This analysis assigns to each of the 16 energy bins independent parameters X_k ($k=1,\ldots,16$) and minimizes the χ^2 function with respect to these fit parameters X_k and to the normalizations N^j (Ref. 9). The confidence contours are obtained again using a likelihood ratio method and the 90% C.L. is shown in Fig. 13(a) by the dotted line. The two types of analyses yield practically the same limits.

Analysis B. Analysis B differs from Analysis A in using a reactor antineutrino spectrum $S_B(E_\nu)$ [Eq. (7)], which is based on independent β-spectra measurements. The associated positron yields $Y^j{}_B(E_{e^+},L^j,\Delta m^2,\theta)$ follow from Eq. (13) by substituting $S_B(E_\nu)$ for $S(E_\nu)$. This approach introduces into the analysis the absolute normalization or putting it another way, the integrated yield of the antineutrino flux, and therefore retains sensitivity to the mixing angle θ up to the maximum value of Δm^2 consistent with the largest neutrino energy in the decay of fission products. For large mass parameters the structure of the oscillations could no longer be resolved in the spectrum and the oscillation limits depend on the uncertainty in the absolute normalization. Introducing an additional overall normalization factor N with error σ_N ($\sigma_N=6.0\%$; 68% C.L.), which takes into account the uncertainties in normalization common to experiments I–III, we may define the following χ^2 function:

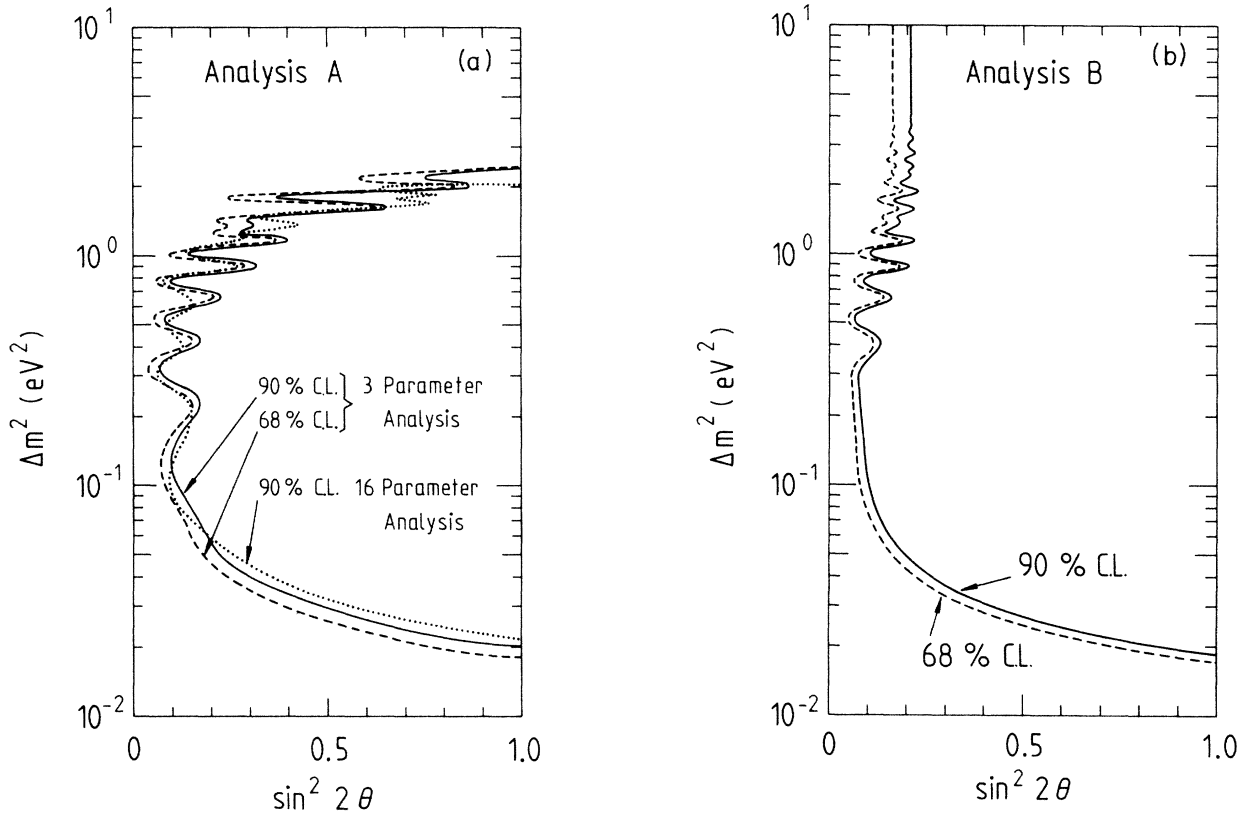

FIG. 13. (a) Exclusion plot for the oscillation parameters Δm^2 and $\sin^2 2\theta$, relying exclusively on the information obtained in experiments I–III. The solid (90% C.L.) and dashed (68% C.L.) curves represent confidence contours of an analysis which relies on the reactor antineutrino spectrum $S_A(E_\nu)$ obtained from the best common fit to experiments I–III. The dotted curves give the 90% C.L. for another analysis which uses independent parameters for each energy bin to characterize a positron spectrum (Sec. VI C). The areas to the right of the curves are excluded. The result is consistent with the absence of neutrino oscillations. (b) Exclusion plot for the oscillation parameters Δm^2 and $\sin^2 2\theta$, combining the results of experiments I–III with measured detector efficiencies, the reaction cross section (neutron half-life 622 sec) and the reactor antineutrino spectrum as derived from independent β-spectra measurements. The result is consistent with the absence of neutrino oscillations.

$$\chi^2(\Delta m^2,\theta)=\sum_j \sum_k \{[Y^j_{\text{expt}}(E_k)-NN^jY_B(gE_k,L^j,\Delta m^2,\theta)]/\sigma_{j,k}\}^2+\sum_j [(N^j-1)/\sigma_j]^2+[(N-1)/\sigma_N]^2+[(g-1)/\sigma_g]^2 , \tag{17}$$

where the gain factor g allows for energy-scale calibration errors. Its uncertainty σ_g is 1.2% (68% C.L.). The χ^2 value for a certain parameter set $(\Delta m^2,\theta)$ was determined by minimizing the χ^2 function in Eq. (17) with respect to the gain factor g and to the normalizations N and N^j. For the case of no oscillations we obtain $\chi^2(0,0)=38.33$ for 48 degrees of freedom (parameter values $N=1.021$, $N_1=0.997$, $N_2=1.009$, $N_3=0.990$, $g=0.986$). Correspondingly we find $\chi^2_{\min}=37.45$ for the parameter values $(\Delta m^2)^*=0.88$ eV^2, $(\sin^2 2\theta)^*=0.057$, $N^*=1.049$, $(N_1)^*=0.998$, $(N_2)^*=1.010$, $(N_3)^*=0.991$, and $g^*=0.986$. To assign relative probabilities to all parameter sets $(\Delta m^2,\theta)$ we have performed a maximum-likelihood test by comparing $\chi^2(\Delta m^2,\theta)$ to $\chi^2_{\min}$ [Eq. (16)]. The probability distribution of the values of the likelihood function is again derived from a Monte Carlo simulation.

The confidence contours for 68% C.L. (dashed curve) and 90% C.L. (solid curve) are represented in Fig. 13(b), where all parameters lying to the right of the curves are excluded. The limit for the mixing angle θ, $\sin^2 2\theta<0.21$ (90% C.L.) depends in the asymptotic range of large mass parameters on the normalization of the predicted positron yields, which in turn depends on the reaction cross section and therefore on quantities such as the neutron half-life.

We obtain, for example, an upper limit of $\sin^2 2\theta < 0.17$ (90% C.L.) by assuming a neutron half-life of $t_{1/2} = 641$ sec, instead of 622 sec.

D. Discussion of the present results

Our confidence in the results of Analysis B is strengthened by the mutual consistency between the reactor antineutrino spectrum $S_A(E_\nu)$ derived exclusively from the fit of the three measured positron spectra (Sec. VI C), and the spectrum $S_B(E_\nu)$ derived essentially from β-spectroscopic data (Sec. III A). The corresponding positron yields are shown in Fig. 12(b), where the solid and dashed curves refer to the yields derived from $S_A(E_\nu)$ and $S_B(E_\nu)$, respectively, assuming no oscillations. The experimental data points of experiments I–III are shown likewise. It should be stressed that the solid curves in Fig. 12(b) represent positron energy distributions obtained from the best fit (assuming no oscillations) of one common reactor antineutrino spectrum to all three measurements at positions L^j. The three solid curves are (apart from trivially different solid-angle factors) essentially identical with very small differences caused by minor changes in fuel composition, detector efficiencies, and reactor power. The internal consistency of our measurements performed at the three distances L^j is reflected in the good agreement between the solid curve and the data points. Support to the no-oscillation hypothesis is given by the way in which the dashed curve describes the data points.

VII. DISCUSSION AND CONCLUSIONS

In the present experiment we have investigated the possible presence of neutrino oscillations in an effort to obtain information on the neutrino mass parameters and on neutrino mixing. Our measurements at Gösgen do not show evidence for neutrino oscillations in a large area of the oscillation-parameter space. For large mass parameters we find that the mixing angle $\sin^2 2\theta$ cannot exceed the value of 0.21 (90% C.L.), while the mass parameter Δm^2 has an upper limit of 0.19 eV^2 (90% C.L.) for maximum mixing. With the present equipment these limits can hardly be improved. The sensitivity to the mass parameter could conceivably be extended down to $\Delta m^2 \approx 10^{-3}$ eV^2 with a different and larger detector, which makes up for the diminishing ratio between signal and background at large distances L. It seems difficult, however, to improve on the sensitivity to the mixing parameter $\sin^2 2\theta$, which is limited by systematic errors such as uncertainties in the detector efficiency, the reaction cross section (neutron half-life), the reactor antineutrino spectrum, and the reactor power. Reactor-based oscillation experiments at two distances have also been reported by a group working at the 2.8-GW (thermal) power reactor in Bugey, France.[26] Their results are indicative of the presence of oscillations with parameters centered around the values $\Delta m^2 = 0.2$ eV^2 and $\sin^2 2\theta = 0.25$. These results are in conflict with our data as discussed in Refs. 10 and 27. In addition results from a one-position measurement at the 1.4-GW (thermal) reactor at Rovno, U.S.S.R. were reported which, although less restrictive, do not show evidence for neutrino oscillations.[28] Similar experiments are in progress at two distances from the core of the 2.3-GW (thermal) Savannah River reactor, U.S.A.[29]

ACKNOWLEDGMENTS

We would like to thank the Aare-Tessin AG für Elektrizität and the Kernkraftwerk Gösgen-Däniken AG for their continuous hospitality. G. Meier and W. Sauser have provided us with the necessary reactor data. Contributions from J. Langhans, E. Baumann, and R. Portmann in technical matters are gratefully acknowledged. Discussions with P. Vogel and K. Schreckenbach were much appreciated. Early contributions of J. Egger, L. Meier, F. Pozar, and P. Tosolini are appreciated. The hospitality of the CERN EP Division is much appreciated. Financial support was obtained from the U.S. Department of Energy and from the Bundesministerium für Forschung und Technologie of the Federal Republic of Germany.

---

*Present address: CERN, CH-1211 Geneva 23, Switzerland.
†Present address: SIN, CH-5234 Villigen, Switzerland.
‡Present address: Bell Communications Research, Red Bank, NJ 07701-7020.
§Present address: UCI, Irvine, CA 92717.
**Present address: Research Laboratories, Eastman Kodak, Rochester, NY 14650.
††Present address: University of Neuchatel, CH-2000 Neuchatel, Switzerland.

[1]K. E. Bergkvist, Nucl. Phys. **B39**, 317 (1972).
[2]R. Abela *et al.*, Phys. Lett. **146B**, 431 (1984).
[3]S. Abachi *et al.*, Phys. Rev. Lett. **56**, 1039 (1986).
[4]S. Boris *et al.*, Phys. Lett. **159B**, 217 (1985); however, see M. Fritschi *et al.*, *ibid.* **173B**, 485 (1986).
[5]See, for example, F. Boehm and P. Vogel, Annu. Rev. Nucl. Part. Sci. **34**, 125 (1984).
[6]B. Pontecorvo, Zh. Eksp. Teor. Fiz. **34**, 247 (1958) [Sov. Phys. JETP 7, 172 (1958)]; S. M. Bilenky *et al.*, Phys. Rep. **41**, 225 (1978).
[7]J. M. Bahcall *et al.*, Rev. Mod. Phys. **54**, 767 (1982).
[8]J. L. Vuilleumier *et al.*, Phys. Lett. **114B**, 298 (1982).
[9]K. Gabathuler *et al.*, Phys. Lett. **138B**, 449 (1984).
[10]V. Zacek *et al.*, Phys. Lett. **164B**, 193 (1985).
[11]H. Kwon *et al.*, Phys. Rev. D **24**, 1097 (1981).
[12]See, for example, T. Yamazaki *et al.*, in *Neutrino '84*, proceedings of the 11th International Conference on Neutrino Physics and Astrophysics, Dortmund, 1984, edited by K. Kleinknecht and E. A. Paschos (World Scientific, Singapore, 1984), p. 183; K. Schreckenbach *et al.*, Phys. Lett. **129B**, 265 (1983); J. Markey *et al.*, Phys. Rev. C **32**, 2215 (1985).
[13]CHARM Collaboration, J. Dorenbosch *et al.*, Phys. Lett. **166B**, 473 (1986).

[14]G. Meier and W. Sauser (private communication).
[15]M. F. James, J. Nucl. Energy **23**, 517 (1969); J. M. Paratte, Swiss Federal Institute for Reactor Research, Report No. TM-45-81-19 (unpublished).
[16]F. V. Feilitzsch *et al.*, Phys. Lett. **118B**, 162 (1982); K. Schreckenbach *et al.*, Phys. Lett. **160B**, 325 (1985).
[17]P. Vogel *et al.*, Phys. Rev. C **24**, 1543 (1981).
[18]P. Vogel, in *First Aspen Winter Conference*, proceedings, Aspen, 1985, edited by Martin M. Block (Ann. N.Y. Acad. Sci. 461) (New York Academy of Sciences, New York, 1986), p. 582.
[19]H. V. Klapdor *et al.*, Phys. Rev. Lett. **48**, 127 (1982).
[20]H. Yamaguchi, Prog. Theor. Phys. **23**, 1117 (1960).
[21]D. H. Wilkinson, Nucl. Phys. **A377**, 474 (1982).
[22]Particle Data Group, Rev. Mod. Phys. **56**, S1 (1984).
[23]P. Vogel, Phys. Rev. D **29**, 1918 (1984); S. A. Fayans, Yad. Fiz. **42**, 929 (1985) [Sov. J. Nucl. Phys. **42**, 590 (1985)].
[24]G. Zacek, thesis, Technische Universität München, 1984 (unpublished).
[25]F. James, in *1982 CERN School of Computing*, proceedings, Zinal, Switzerland, 1982 (CERN, Geneva, 1983), p. 182.
[26]J. F. Cavaignac *et al.*, Phys. Lett. **148B**, 387 (1984).
[27]F. Boehm, in *Current Problems in Nuclear Physics*, edited by T. Paradellis and S. Kossionides (Hellenic Phys. Soc. Conf. Series 1) (Hellenic Physical Society, Athens, 1986), p. 67.
[28]A. Afonin *et al.*, Pis'ma Zh. Eksp. Teor. **42**, 230 (1985) [JETP Lett. **42**, 285 (1985)].
[29]H. Sobel, in *Proceedings of the 6th Moriond Workshop on Massive Neutrinos in Particle Physics and Astrophysics, 1986*, edited by O. Fackler and J. Tran Thanh Van (Editions Frontières, Paris, 1986), p. 339.